

# Toward Accurate and Accessible Markerless Neuronavigation

Ziye Xie<sup>a,1</sup>, Oded Schlesinger<sup>a,g,1</sup>, Raj Kundu<sup>b,f,1</sup>, Jessica Y. Choi<sup>b</sup>, Pablo Iturralde<sup>e</sup>, Dennis A. Turner<sup>c,d</sup>, Stefan M. Goetz<sup>a,b,c</sup>, Guillermo Sapiro<sup>g</sup>, Angel V. Peterchev<sup>a,b,c,d,2</sup>, J. Matias Di Martino<sup>a,e,2</sup>

<sup>a</sup>*Department of Electrical and Computer Engineering, Duke University, 27708, NC, USA*

<sup>b</sup>*Department of Psychiatry & Behavioral Sciences, Duke University, 27710, NC, USA*

<sup>c</sup>*Department of Neurosurgery, Duke University, 27710, NC, USA*

<sup>d</sup>*Department of Biomedical Engineering, Duke University, 27708, NC, USA*

<sup>e</sup>*Universidad Católica del Uruguay, 11600, Uruguay*

<sup>f</sup>*Boston University School of Medicine, 02118, MA, USA*

<sup>g</sup>*Department of Electrical and Computer Engineering, Princeton University, 08544, NJ, USA*

---

## Abstract

Neuronavigation is widely used in biomedical research and interventions to guide the precise placement of instruments around the head to support procedures such as transcranial magnetic stimulation. Traditional systems, however, rely on subject-mounted markers that require manual registration, may shift during procedures, and can cause discomfort. We introduce and evaluate markerless approaches that replace expensive hardware and physical markers with low-cost visible and infrared light cameras incorporating stereo and depth sensing combined with algorithmic modeling of the facial geometry. Validation with 50 human subjects yielded a median tracking discrepancy of only 2.32 mm and 2.01° for the best markerless algorithms compared to a conventional marker-based system, which indicates sufficient accuracy for transcranial magnetic stimulation and a substantial improvement over prior markerless results. The results suggest that integration of the data from the various camera sensors can improve the overall accuracy further. The proposed markerless neuronavigation methods can reduce setup cost and complexity, improve patient comfort, and expand access to neuronavigation in

---

<sup>1</sup>Contributed equally to this work.

<sup>2</sup>Contributed equally to this work.

clinical and research settings.

*Keywords:* Markerless tracking, Pose estimation, Head shape modeling, Neuronavigation, TMS.

---

## 1. Introduction

Accurate and robust subject tracking is critical in research and clinical interventions involving brain recording and stimulation. These procedures are typically supported by neuronavigation systems that guide practitioners in targeting specific areas of the brain. The application of neuronavigation, facilitated by the continuous monitoring of a subject's position and orientation, is critical in a variety of procedures. These include precise targeting of brain regions during transcranial magnetic stimulation (TMS) [1], accurate placement and registration of electroencephalography (EEG) electrodes [2], image-guided surgery [3], and localization of epileptogenic loci and tumors [4, 5]. Due to the density and complexity of brain tissue, these applications necessitate high accuracy and robustness of neuronavigation to ensure treatment consistency and efficacy.

A typical hardware configuration for neuronavigation systems incorporates a pair of infrared (IR) cameras as the primary tracking device, which localizes passive retroreflective markers in 3D space [6, 7] (see, e.g., Figure 1). Alternatively, the markers comprise powered electromagnet coils that are tracked with a magnetic field sensor [8]. Such physical markers are rigidly attached to the objects of interest, e.g., a patient's head and a TMS coil, and registered manually using a calibration procedure [9]. While the highest tracking accuracy is achieved through rigid fixation to the cranium using stereotactic frames (e.g., Leksell [10]) or skull screws (e.g., Nexframe [11]) to eliminate errors caused by the skin shifting several millimeters relative to the skull [12], such methods are limited to invasive interventions. Consequently, marker attachment to human subjects is commonly implemented with goggles, elastic headbands, or adhesive pads applied to the skin. The registration process commonly entails manual identification of specific anatomical landmarks and subsequent establishment of the spatial relationship between these landmarks and the markers using a pointing device [8]. Following this registration, the neuronavigation system can infer the position and orientation of the objects of interest by tracking the affixed physical markers.

Factors limiting the accuracy and robustness of neuronavigation-guided

procedures stem from their dependence on physical markers and the manual registration protocols, as well as the lack of personalized head models and head 3D scanning. The premise of precise localization of a tracked object is the rigid attachment of the markers to the subject; however, markers are susceptible to displacement [13, 14] and may exhibit drift throughout a procedure [8, 15]. In addition, the use of adhesive pads might introduce patient discomfort or induce allergic reactions [16, 17], while alternatives such as goggles and elastic bands may not be able to maintain rigid attachment to the subject. Beyond the limitations introduced by physical markers, the manual registration of anatomical landmarks is a time-consuming and error-prone process that introduces human error [18] and is susceptible to displacement of soft tissues when pressed by a pointer [8]. These discrepancies may lead to significant reductions in tracking performance, and the reliance of neuronavigation systems on specialized markers and tracking sensors significantly increases cost and limits their widespread adoption.

To address these limitations, we study computer vision-based techniques for a neuronavigation system that leverages the human face as a natural tracker to develop accurate and comfortable head tracking methods. We developed a multi-modal hardware setup (described in detail in S.1.1) to examine different methods employing recent advances in face detection, facial landmark localization, and 3D head statistical modeling to track human subjects' head movements and compare them to data captured by a conventional neuronavigation system. This work establishes the foundation for an accurate and robust markerless neuronavigation system, with the potential to reduce human error and setup complexity while simultaneously lowering the financial barriers associated with neuronavigation.

The contributions of this work include (i) a computer vision method for subject head tracking in neuronavigation that leverages both color (RGB) and depth (D) information from a single consumer-grade RGB-D device, (ii) an alternative approach that relies on stereo color information captured by a pair of consumer-grade RGB cameras, (iii) a controlled and systematic evaluation of the proposed computer vision-based methods in comparison with a conventional neuronavigation solution, including an extensive experimental assessment of the proposed methods on a cohort of 50 human subjects in a treatment-suite environment.

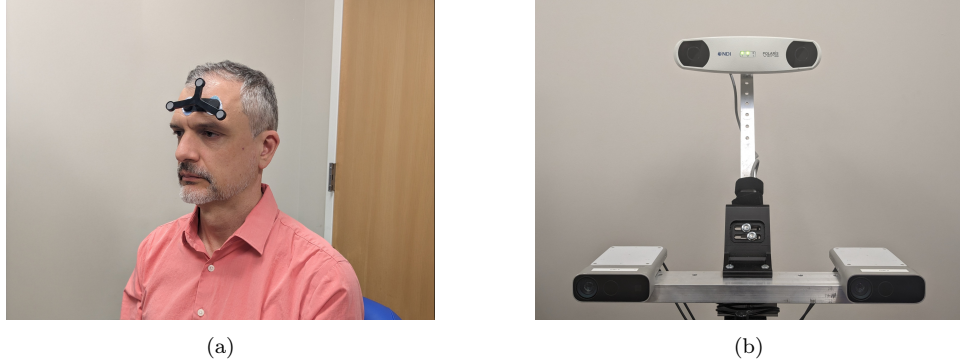


Figure 1: Illustration of conventional marker-based and proposed markerless neuronavigation setups. (a) A subject wearing a tracker with retroreflective markers used by commercial neuronavigation systems. (b) Experimental apparatus developed in this work, consisting of two Azure Kinect DK cameras that capture color and depth data for markerless tracking (bottom) and, for comparison, a standard NDI Polaris Vicra stereotaxy camera tracking the retroreflective markers (top).

## 2. Related Work

A growing body of research has explored markerless tracking approaches as a solution to the limitations of conventional marker-based neuronavigation systems. Several studies have focused on replacing physical markers with anatomical registration techniques using facial geometry. Chiurillo et al. [19] demonstrated a markerless optical neuronavigation system based on CT scans and 3D images registration of facial anatomy, while Kögl et al. [20] proposed a markerless monocular-camera approach for annotating fiducial landmarks to facilitate subject registration. Other works have used augmented reality platforms to integrate facial landmark-based registration with head-mounted self-localization systems [21], and Sathyanarayana et al. [22] compared marker-based vs. markerless tracking in mixed-reality neuronavigation, which supported the clinical relevance of markerless methods. Beyond these approaches, other lines of work have explored computer-vision frameworks that exploit anatomical structures and features for markerless tracking. Manni et al. [23] proposed a method for optical-image pre-processing in spinal surgery by detecting anatomical landmarks and matching local invariant features, whereas Liu et al. [24] introduced an automatic image-to-patient registration system for neurosurgical interventions for efficient alignment of preoperative imaging and real-time patient anatomy. Zeng et al. [25] demonstrated markerless event-by-event motion correction in brain PET imaging

utilizing stereo IR cameras to capture 3D facial surfaces. Huang et al. [26] introduced a joint 3D tracking framework that leverages multi-view RGB-D input to capture detailed poses of humans and objects in contact-rich scenarios. Similarly, Cuevas et al. [27] proposed a multi-view markerless motion capture pipeline for modeling two-person interaction dynamics via parametric body shape estimation. These methods demonstrate the potential of integrating computer-vision techniques to replace traditional marker-based registration and tracking in biomedical context.

Recent studies have demonstrated the feasibility of employing the Azure Kinect DK in a range of clinical applications, including human body motion analysis [28], subject positioning [29], and joint motion and angle tracking [30]. Notably, the Azure Kinect DK is available at a relatively low cost of \$399 (2025 retail price), positioning it as a scalable alternative to specialized tracking hardware. However, its application to head tracking for neuronavigation, particularly in light of the associated high-precision requirements, remains an active area of research.

To the best of our knowledge, the closest work to ours is a study by Matsuda et al. [31], which used monocular RGB data from one subject to estimate head pose through visible facial landmarks and demonstrated its potential for a markerless neuronavigation system. Our study advances significantly beyond this initial effort by incorporating several key improvements. First, our work evaluates the performance of additional hardware modalities, including stereo and depth video data. Second, we incorporate a denser set of facial landmarks and models. Third, we compare the efficacy of facial statistical priors, including a generic face model and a more individualized, statistical prior-based head model. Fourth, we conduct a comprehensive evaluation of the proposed methods in a large cohort of 50 subjects, including comparison with standard neuronavigation hardware, for a robust assessment of accuracy and generalizability.

### 3. Methods

#### 3.1. Tracking Methods

We tracked the pose of the subject’s head using a combination of the RGB and depth data from the two Azure devices (see Figure 2). Each of the two Azure devices acquired two different data modalities: a color image and a point cloud from the RGB camera and the depth sensor, respectively. We

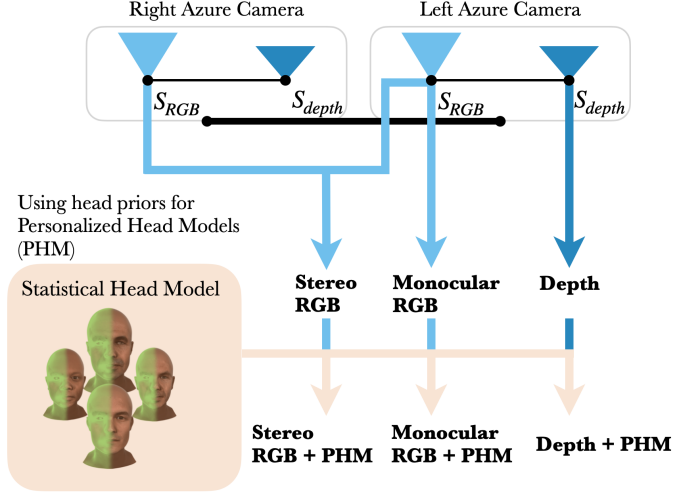


Figure 2: The markerless tracking system comprises a pair of Azure Kinect DK devices. The devices are synchronized and spatially calibrated (thick horizontal black line). Each device contains an RGB and a depth camera (labeled as  $S_{RGB}$  and  $S_{depth}$ , respectively), operating simultaneously (thin horizontal black lines). We implemented and compared three neuronavigation markerless tracking strategies: Monocular RGB (Section 3.1.2), Stereo RGB (Section 3.1.3), and Depth (Section 3.1.4). We compared these techniques with and without the use of statistical head priors (Section 3.2), leading to a final set of six tracking alternatives. The illustration of the statistical head models is adapted from Ploumpis et al. [32].

exploited this multimodal information to compare three tracking methodologies: tracking through a single RGB camera (Monocular RGB), a stereo RGB camera pair (Stereo RGB), and a depth sensor (Depth). Moreover, we explored the use of statistical head priors to regularize the problem of head shape estimation, leading to a final set of six tracking alternatives (each of the three defined above with and without the use of statistical head priors).

### 3.1.1. Notation

In this study, we use the following notation conventions: camera and world points of interest are represented in homogeneous coordinates (see Hartley and Zisserman [33] for details) and denoted using bold lowercase variables, e.g.,  $\mathbf{w} = (u, v, 1)^T$  represents the  $(u, v)$  pixel coordinates in a given camera sensor, and  $\mathbf{x} = (x, y, z, 1)^T$  represents the  $(x, y, z)$  world coordinates in a given reference frame. When the reference frame is not obvious by context, we will introduce a subindex to specify it (see, e.g., Fig-

(a) Camera and world reference frames (b) Our system, subject, and NDI reference frames

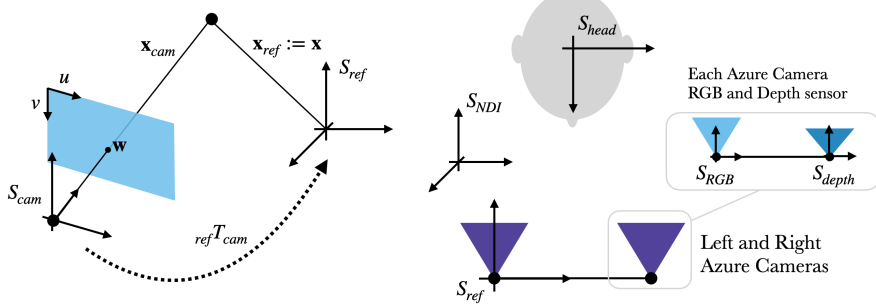


Figure 3: Notation: we adopt a pinhole camera model to represent the geometry of the captured data in the camera and reference coordinate frames, denoted as  $S_{cam}$  and  $S_{ref}$ , respectively, (see (a)). 3D transformations between frames is represented as  $destinationT_{source} := S_{source} \rightarrow S_{destination}$ . Each Azure device has two sensors and associated coordinate frames (RGB and depth) (see (b)). In addition, the head keypoint will be represented in a coordinate frame fixed to the head ( $S_{head}$ ). External data collected for validation, e.g., with a commercial standard NDI system (see Section 3.4 for details), has its own reference frame ( $S_{NDI}$ ). Subindices will be used to denote the reference frame in which points, sets of points, and point clouds are expressed. See Section 3.1.1 for details.

ure 3). Ordered sets of points, such as the set of all landmarks corresponding to a face, are denoted using uppercase variables both in 2D and 3D, e.g.,  $W = [\mathbf{w}_1, \mathbf{w}_2, \dots, \mathbf{w}_n]$  and  $X = [\mathbf{x}_1, \mathbf{x}_2, \dots, \mathbf{x}_n]$ . Unordered collections of points, such as point clouds, are denoted using calligraphic notation, e.g.,  $\mathcal{X} = \{\mathbf{x}_1, \mathbf{x}_2, \dots, \mathbf{x}_n\}$ .

Five distinct reference systems are considered, each identified by a unique subscript. The first three are used in our tracking algorithms: one corresponding to the left Azure sensor ( $S_{cam}$ ), one corresponding to the right Azure sensor ( $S_{right}$ ), and one corresponding to the tracked subject's head ( $S_{head}$ ). Since each Azure device contains two sensors (RGB and depth), each with its own coordinate frame, we define the RGB frame as the primary reference frame for each device, mapping depth data to the RGB frame when necessary (see Figure 3). We define  $S_{cam}$  as the worldview reference frame. The other two systems are employed by the reference NDI Polaris Vicra (Northern Digital Inc) system, which we use for comparison: the NDI sensor's coordinate system ( $S_{NDI}$ ) and one corresponding to the retroreflective marker set that the NDI system tracks ( $S_{markers}$ ). We will also use subscripts to denote the reference system in which points, sets of points, and point clouds are expressed. For example,  $\mathbf{X}_{cam}$  refers to a set of points described

in the reference system  $S_{cam}$ , and when no reference system is specified, we assume the reference system  $S_{ref}$ . Transformations between reference frames are noted as  $destination T_{source} := S_{source} \rightarrow S_{destination}$ , and are represented by a  $4 \times 4$  (rotation and translation) transformation  $T = [R|\mathbf{t}]$  in homogeneous coordinates. We define the set of transformations as the Euclidean group,

$$SE(3) = \left\{ \begin{bmatrix} R & t \\ 0 & 1 \end{bmatrix} \mid R \in SO(3), t \in \mathbb{R}^3 \right\}, \quad (1)$$

where  $SO(3)$  is the set of rotation matrices, i.e., orthogonal with determinant 1. Hartley and Zisserman [33] provide additional details on 3D transformations in homogeneous coordinates.

### 3.1.2. Monocular RGB-Based Tracking

Perspective-n-Point (PnP) algorithms are extensively used methods for monocular object pose estimation [34, 35, 36, 37]. These algorithms are provided with a set of two-dimensional keypoint locations  $W$  as input and assume a known 3D geometry model with corresponding 3D keypoints  $X$ . The 3D location of the object of interest was estimated by minimizing the 2D reprojection discrepancy between  $X$  and  $W$ . In the context of head pose estimation, given an RGB image, these methods require detecting a set of facial landmarks, as described in the following.

**Face Detection and Landmark Localization.** Face detection and facial landmark localization were performed using the MediaPipe [38] framework, which provided and localized 468 facial landmarks (Figure 4). Facial landmarks associated with areas of the face that are visually salient and have strong semantic definition (e.g., the corner of the eyes) tend to be more reliably localized, as they suffer less from annotation ambiguity compared to weakly defined landmarks along contours [39]. We empirically identified and selected a subset of salient facial landmarks (Figure 4(c)). For details on the selection of this optimal set and ablation studies, see S.3. We will refer to this subset of landmarks as the MediaPipe-Subset  $W/X$ , where, as before,  $W$  and  $X$  respectively denote the set of pixel  $\mathbf{w}_i$  and 3D  $\mathbf{x}_i$  coordinates.

**Pinhole Camera Model and PnP Formulation.** For each RGB camera, we calculated the projection matrix  $P$  through standard camera calibration procedures (see S.1.3). This allowed us to project world 3D coordinate points into the camera pixel space, i.e.,  $z\mathbf{w} = P\mathbf{x}$ , where  $z$  is a

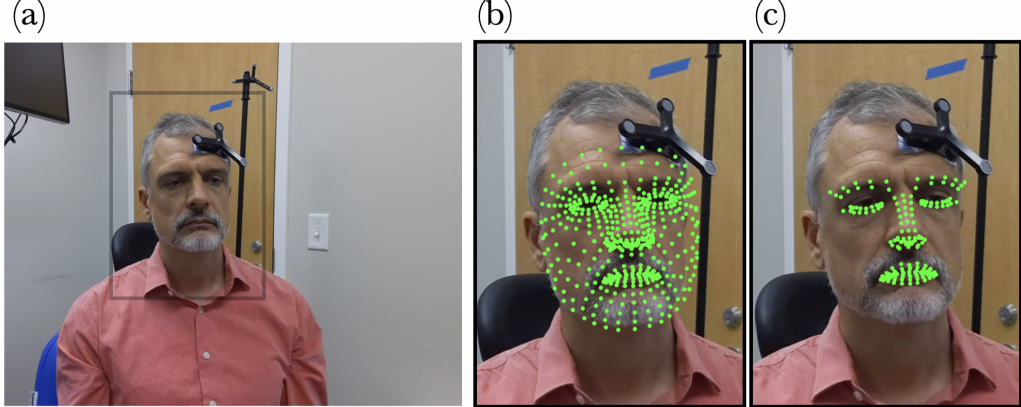


Figure 4: (a) Sample RGB input frame from the reference Azure camera (left camera), (b) set of MediaPipe facial landmarks detected in the frame, and (c) subset of landmarks used for tracking (for details on landmark selection and ablation studies, see S.3).

scalar factor representing point depth along the optical axis of the camera. The canonical formulation assumes 3D vectors are described in the camera frame; the reprojection equation can be generalized to any reference frame  $ref$  by including a transformation between the reference and camera frame, i.e.,  $z\mathbf{w} = P_{cam}T_{ref}\mathbf{x}_{ref}$  (Figure 3).

The monocular pose estimation problem can be formulated as finding the transformation matrix  $_{ref}T_{head}$  defined by the optimization problem:

$$_{cam}T_{head} = \operatorname{argmin}_{T \in SE(3)} \|W - \sigma(PTX^{\text{template}})\|^2, \quad (2)$$

where  $X^{\text{template}}$  refers to the matrix of all the 3D facial landmarks for a given face model (in this case MediaPipe) expressed in the canonical head reference frame, and  $W$  is the matrix of the landmark locations observed by the camera in pixel form. The operator  $\sigma()$  refers to the normalization of a matrix column-wise using its last row to project numerical solutions into its homogeneous coordinates (see Hartley and Zisserman [33] for details).

### 3.1.3. Stereo RGB-Based Tracking

The spatial location of a point can be determined through the principle of stereo triangulation [33]. This method infers 3D depth information via 2D pixel point correspondence. We applied this principle to reconstruct the 3D coordinates of a set of distinct facial landmarks identified in the pair of RGB cameras available in each Azure device (see Figure 2). We modeled

the head as a rigid body; hence, we can estimate the head pose by finding the optimal transformation that aligns the estimated 3D landmark locations with a reference 3D face model.

Initially, the 2D pixel coordinates of a set of MediaPipe landmarks were estimated for both the left and the right RGB images, as described in Section 3.1.2. We denote  $\mathbf{w}_{\text{left}}$  and  $\mathbf{w}_{\text{right}}$  the 2D pixel coordinates detected in the left and right RGB cameras for one landmark (we have as many vector pairs as landmarks, see S.3.1 for a discussion on the landmark set selection). The RGB cameras were calibrated (see S.1.3 for details) to obtain the projection matrices  $P_{\text{left}}$  and  $P_{\text{right}}$ . As stated in Section 3.1.1, we used the left camera system as the global reference system, meaning  $P_{\text{left}} = K_{\text{left}}[[\text{Id}_{3 \times 3}, [0 \ 0 \ 0]] | [0 \ 0 \ 0 \ 1]^T]$ , and  $P_{\text{right}} = K_{\text{right}} T_{\text{left}}$ , where  $K_{\text{left}}$  and  $K_{\text{right}}$  are the intrinsic calibration matrices of the left and right cameras, respectively, and  $T_{\text{left}}$  is the transformation between the left and right camera systems. Then, the location of each landmark in the 3D world  $\mathbf{x}$  was obtained by solving:

$$\mathbf{w}_{\text{left}} \times P_{\text{left}} \mathbf{x} = 0, \quad \mathbf{w}_{\text{right}} \times P_{\text{right}} \mathbf{x} = 0. \quad (3)$$

Equation 3 can be rearranged into a linear system of equations whose solution is obtained through Singular Value Decomposition (SVD) [33]. This procedure was repeated for each landmark to obtain a set of 3D points expressed in the left camera reference frame, denoted as  $X$  (each column representing the 3D homogeneous coordinates of a facial landmark).

With the 3D landmarks reconstructed, the head pose was estimated by finding the optimal transformation that aligns a template 3D face model to these landmarks:

$${}_{\text{ref}} T_{\text{head}} = \operatorname{argmin}_{T \in SE(3)} \|X - (T X^{\text{template}})\|^2, \quad (4)$$

where  $X^{\text{template}}$  is, similar to Equation 2, the matrix with the 3D coordinates of the selected landmarks in the (MediaPipe) facial model.

### 3.1.4. Depth-Based Tracking

The third method presented here utilizes depth data from the reference Azure device to track the subject’s head. For each frame, a point cloud  $\mathcal{X}$  was obtained from the depth sensor and used to estimate the transformation that aligns a reference facial geometry to the captured point cloud corresponding

to that frame. Unlike previous methods, which relied on sparse sets of landmarks, this method leverages the full dense point cloud data captured by the depth sensor. Construction of the reference 3D template for head-pose estimation is described next.

We defined a subject-specific facial template using data captured during a brief ( $<1$  minute) initial session. In each (RGB) frame, we detected MediaPipe facial landmarks  $\{\mathbf{w}_i\}$  and mapped these to their corresponding 3D points in the point cloud  $\mathbf{x}_i \in \mathcal{X}$ . This was accomplished using functionalities provided by the Azure device’s Software Development Kit (SDK) for mapping across the RGB and depth sensors [40]. The convex hull of MediaPipe landmarks is used to define the facial region of interest, as shown in Figure 5. Point clouds acquired from the scanning session were co-registered through a two-step alignment procedure. An initial coarse alignment is established based on landmark correspondences, which is subsequently refined using ICP [41]. Following registration, a facial template was obtained by averaging all aligned point clouds. This facial template is then used as the reference geometry for depth-based tracking.

Once a facial 3D template  $\mathcal{X}^{\text{template}}$  was defined, we tracked the movement of the head by aligning new data  $\mathcal{X}$  to the template (which is represented in the reference frame) per

$${}_{\text{ref}}T_{\text{head}} = \operatorname{argmin}_{T \in SE(3)} d_{\text{Chamfer}}(\mathcal{X}, T \mathcal{X}^{\text{template}}), \quad (5)$$

where  $d_{\text{Chamfer}}(\mathcal{X}_1, \mathcal{X}_2)$  is the Chamfer distance between two point clouds  $\mathcal{X}_1$  and  $\mathcal{X}_2$ , defined as

$$d_{\text{Chamfer}}(\mathcal{X}_1, \mathcal{X}_2) = \frac{1}{|\mathcal{X}_1|} \sum_{\mathbf{x}_1 \in \mathcal{X}_1} \min_{\mathbf{x}_2 \in \mathcal{X}_2} \|\mathbf{x}_1 - \mathbf{x}_2\|_2^2 + \frac{1}{|\mathcal{X}_2|} \sum_{\mathbf{x}_2 \in \mathcal{X}_2} \min_{\mathbf{x}_1 \in \mathcal{X}_1} \|\mathbf{x}_2 - \mathbf{x}_1\|_2^2. \quad (6)$$

### 3.1.5. Comparison to Prior Markerless Tracking Method

To benchmark the performance of the proposed methods against prior art in markerless tracking in neuronavigation settings, we included a comparison with the MarLe algorithm proposed by Matsuda et al. [31]. MarLe functions as a monocular RGB tracking approach. Unlike the method described in Section 3.1.2, which utilizes MediaPipe, MarLe employs the Dlib library to detect facial landmarks. As the source code for MarLe is currently unavailable to the public, we re-implemented the method closely following the description in the original paper. Moreover, the original MarLe study used

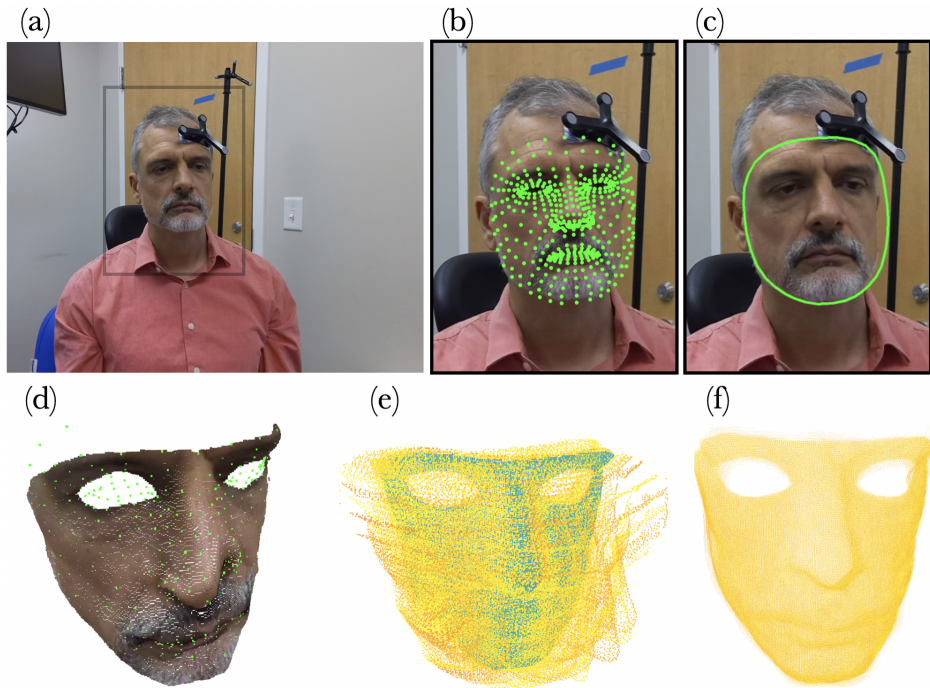


Figure 5: Creation of the 3D facial template for point cloud tracking. (a) Sample RGB input frame. (b) MediaPipe landmarks detected in the RGB image. (c) Convex hull of the landmarks used to define the facial region of interest. (d) Color information is mapped into the 3D reference frame to select the point cloud region of interest, and locate 3D landmarks. (e) Several point clouds obtained during a scanning session are aligned and merged to define the facial 3D template (shape). (f) Reference facial 3D template.

video data with resolutions of  $2048 \times 1536$ ,  $1920 \times 1080$ , and  $1280 \times 720$  [31], whereas in this study, we used data with a higher resolution of  $3840 \times 2160$ , and therefore the performance of this algorithm is expected to be superior in our study compared to the original. While we could have downsampled our video data to match the resolution in the MarLe original study, our focus was on the comparison of the markerless algorithms rather than the camera hardware.

### 3.2. Personalized Head Model (PHM) Leveraging Statistical Priors

All three tracking methods introduced above (Monocular RGB, Stereo RGB, and Depth) were enhanced by leveraging statistical head priors. These priors provide two key advantages in the context of TMS. First, they help regularize the template facial estimation by leveraging prior knowledge of the human head shape [32, 42]. Second, they provide a complete head representation, allowing us to track any target point on the face or scalp [32, 43, 44, 45].

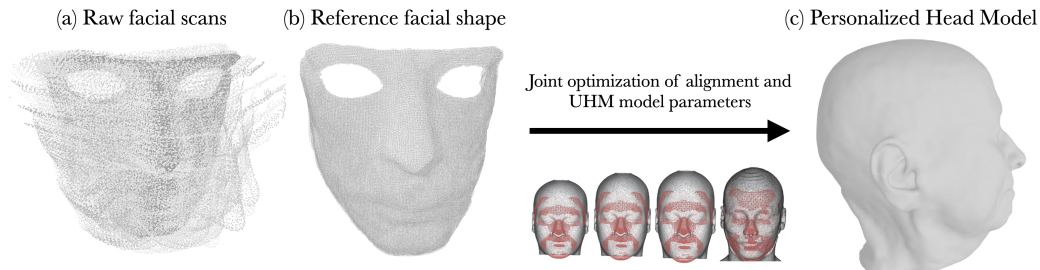


Figure 6: Personalized Head Model (PHM) created by fitting a 3D morphable model to a subject-specific facial template (see Section 3.1.4). The PHM provides a complete and annotated representation of the subject’s head and face geometry. It is obtained by jointly aligning and optimizing the model parameters, see S.4 and Schlesinger et al. [43] for optimization details.

The PHM was constructed by fitting a three-dimensional morphable model (3DMM) called the Universal Head Model (UHM) [32, 46] to a set of face scan point clouds. The UHM is a statistical model with a fine-detailed and complete representation of the human head structure, encompassing a broad range of subject variations. It has been annotated with the 68 Multi-PIE (pose, illumination, and expression) facial landmarks established by Gross et al. [47] and commonly used by the Dlib library, and with the International 10–20 System neurocranial landmarks [48].

The creation of the PHM for each subject involved a two-stage process. First, we created a personalized facial template as described in Section 3.1.4 and illustrated in Figure 5. Subsequently, we fitted the UHM model to this facial template by jointly optimizing a transformation and the model’s coefficients, as described in detail in our previous work [43]. The result is a personalized and regularized complete facial and head representation  $\mathcal{X}^{PHM}$  as illustrated in Figure 6.

With this PHM, we implemented a second version of each of the three approaches described before (Monocular RGB, Stereo RGB, and Depth), where the PHM now defines the reference facial geometry. Monocular RGB + PHM is defined by modifying Equation 2 to use the position of the keypoints from the PHM instead of MediaPipe. Similarly, Stereo RGB + PHM is defined by modifying Equation 4 to replace the MediaPipe keypoints  $X^{template}$  with the PHM ones. Finally, Depth + PHM is defined by modifying Equation 5 to use the PHM point cloud  $\mathcal{X}^{PHM}$  as  $\mathcal{X}^{template}$ .

### 3.3. Study Participants

The human subjects study was approved by the Duke University Health System Institutional Review Board (Pro00109130). Fifty healthy participants completed the study (27 female, 23 male, 20–76 years old, with a mean of 28.6). Effort was made to recruit participants of various racial and ethnic backgrounds (see Table S.1) to capture a diverse set of facial features for robust development and evaluation of the tracking algorithms.

### 3.4. Experimental Setup

Participants were seated in front of the data collection apparatus shown in Figure 1, which consists of an NDI Polaris Vicra stereotaxy camera (*NDI*) on top of a pair of calibrated Microsoft Azure Kinect DK (*Azure*) devices. The NDI stereotaxy camera tracked a Brainsight Subject Tracker tool (*subject tracker*; Rogue Research Inc.), whereas the Azure devices operated with wired synchronization, independently of the NDI camera. S.1 provides further configuration details. Collectively, time-synchronized and spatially co-registered data streams were recorded with one RGB and depth stream coming from each Azure device.

For each participant, a pair of recordings was acquired: a face scan recording and a recording for tracking accuracy comparisons. During these sessions, participants were instructed to maintain a neutral facial expression while performing a series of controlled head movements. Concurrent data

acquisition was performed using both the NDI and Azure systems. In the first recording, subjects were instructed to perform two sets of clockwise and counterclockwise head roll movements. This recording facilitated the comprehensive facial data acquisition by the Azure camera system and is referred to as the “face scan recording.” After the face scan recording, a retroreflective subject tracker was affixed to the forehead of subjects with adhesive EEG snap electrodes as shown in Figure 1(a), following standard practice for TMS neuronavigation. Subsequently, subjects were instructed to replicate eight different head movements by following along in real time to a demonstration video. These movements include translation (sway, surge, and heave) and rotation (roll, pitch, and yaw), as well as combined pitch and yaw rotations for clockwise and counterclockwise head roll movements. This second recording was used for tracking accuracy analysis and is referred to as the “tracking comparison recording.”

Frames in which the operator inadvertently obscured the subject from the data collection apparatus, or when the retroreflective markers detached from the forehead of the subject due to failure of the adhesive electrode pads, were excluded from further analysis. These issues were observed in data from six subjects (out of 50), and the average frame exclusion rate in those six videos was 22.4%. The remaining data (44 subjects) had no frame exclusion.

### *3.5. Performance Characterization*

Performance of the tracking methods was evaluated through a comparison to the standard marker-based infrared camera system (NDI). Since the reference (NDI) and our tracking data were independently collected and represented in different reference frames (see, e.g., Figure 3), pose estimates have to be synchronized and spatially aligned before comparison. Next, we describe the synchronization and spatiotemporal alignment procedure, followed by the performance characterization methods.

#### *3.5.1. Synchronization and Spatiotemporal Alignment*

For both temporal and spatial alignment, we used the trajectory of the retroreflective subject tracker as a common signal, as it could be tracked by both systems (see Green et al. [49] for details on how our system detects and tracks the retroreflective markers). Temporal alignment was achieved by maximizing the cross-correlation between the two data streams. Since the transformation between our reference system and NDI’s ( $_{NDI}T_{cam}$ ) did not vary in time (i.e., the Azure setup and the NDI system are fixed in space), we

obtained it by minimizing the difference between the two trajectories after temporal alignment (for details, see Green et al. [49]). Spatial and temporal alignment parameters were simultaneously optimized through a grid search to guarantee optimal convergence. Quaternions were employed throughout this process to represent rotations continuously and mitigate potential singularities associated with Euler angles.

### 3.5.2. Performance Metrics

The primary metrics we report are the root-mean-square discrepancy (RMSD) for the tracking discrepancy in the translation (mm) and angular components ( $^{\circ}$ ). In addition, the robustness of each tracking system was evaluated by analyzing the failure rate, which is defined as the percentage of frames in which a system could not produce valid tracking data. Such failure events were attributed to various factors, including facial landmark detection errors, head pose estimation errors (e.g., when the head was located behind the camera in the PnP algorithm), and occlusions of the tracking target during extreme head orientations.

### 3.5.3. Head Pose Impact Analysis

Since facial analysis tends to be sensitive to head pose [50, 51], to evaluate the robustness of our methods against such variations, we investigated the impact of the subject’s head pose on tracking performance. Specifically, we characterized the head pose using six degrees of freedom: three translational (sway, surge, and heave) and three rotational (roll, pitch, and yaw). For each degree of freedom, we quantified the tracking performance by computing the RMSD of the translation and rotation discrepancies independently. This component-wise breakdown facilitates the identification of specific method shortcomings or movement types that may degrade tracking accuracy, such as depth estimation errors during surge movements or feature occlusion during yaw rotations.

## 3.6. Statistical Analysis

To assess the significance of the differences between the tracking methods, the performance metrics were analyzed with repeated measures (RM) tests reflecting the within-subject study design. Translation and rotation discrepancies served as dependent variables and were log-transformed to reduce skewness prior to statistical analysis. They were first included jointly in an RM multivariate analysis of variance (MANOVA), together with the

proposed six tracking methods and the prior MarLe method [31] (i.e., seven methods in total), reporting Pillai’s trace. Follow-up one-way RM analysis of variance (ANOVA) tests were performed separately for translation and rotation discrepancies, where prior testing of normality and sphericity was conducted using the Shapiro-Wilk test and Mauchly’s test, respectively. Upon violation of sphericity, Greenhouse–Geisser (GG) correction was employed. Due to the violation of normality in rotation discrepancy data, the non-parametric Friedman test was computed for confirmation of the ANOVA results. Following the two one-way RM ANOVA tests, post-hoc paired *t*-tests with Holm correction for multiple comparisons were applied to compare the individual tracking methods. Descriptive statistics such as the mean, median, and interquartile range were computed in log space and back-transformed to the original units. Failure rate was reported for the six proposed methods as well as MarLe and NDI (i.e., totaling eight methods). It was analyzed using the Friedman test due to the strong skewness of the data, followed by a post-hoc pairwise Wilcoxon signed-rank test with Holm correction for multiple comparisons. Results were considered statistically significant for  $p < 0.05$ . Statistical analyses were performed in Python 3.10.12 [52] with multiple packages: RM MANOVA—R 4.5.2 [53] via rpy2 3.6.4 [54]; RM ANOVA and Mauchly’s test—Pingouin 0.5.5 [55]; Holm corrections—statsmodels 0.14.5 [56]; Shapiro-Wilk, Friedman, and Wilcoxon signed-rank tests—Scipy 1.13.1 [57].

## 4. Results

### 4.1. Tracking Performance

The MANOVA revealed a significant effect of the type of markerless tracking method on the translation and rotation discrepancy relative to the standard marker-based tracking system (NDI) (Pillai’s Trace = 0.946,  $F_{6,44} = 129$ ,  $p < 0.0001$ ). There was also a significant tracking method  $\times$  discrepancy metric interaction (Pillai’s Trace = 0.928,  $F_{6,44} = 94.1$ ,  $p < 0.0001$ ), indicating the performance of each method varied differently for translation and for rotation. The subsequent one-way ANOVAs on the two discrepancy metrics confirmed a strong tracking method effect for translation discrepancy ( $\varepsilon_{\text{GG}} = 0.417$ ;  $F_{2.50,123} = 412$ ,  $p < 0.0001$ ,  $\eta^2_{\text{G}} = 0.774$ ) and rotation discrepancy ( $\varepsilon_{\text{GG}} = 0.722$ ;  $F_{4.33,212} = 126$ ,  $p < 0.0001$ ,  $\eta^2_{\text{G}} = 0.619$ ). The latter was confirmed with a Friedman test ( $\chi^2_6 = 232$ ,  $p < 0.0001$ ; Kendall’s  $W = 0.773$ ) because residual normality was violated (Shapiro–Wilk

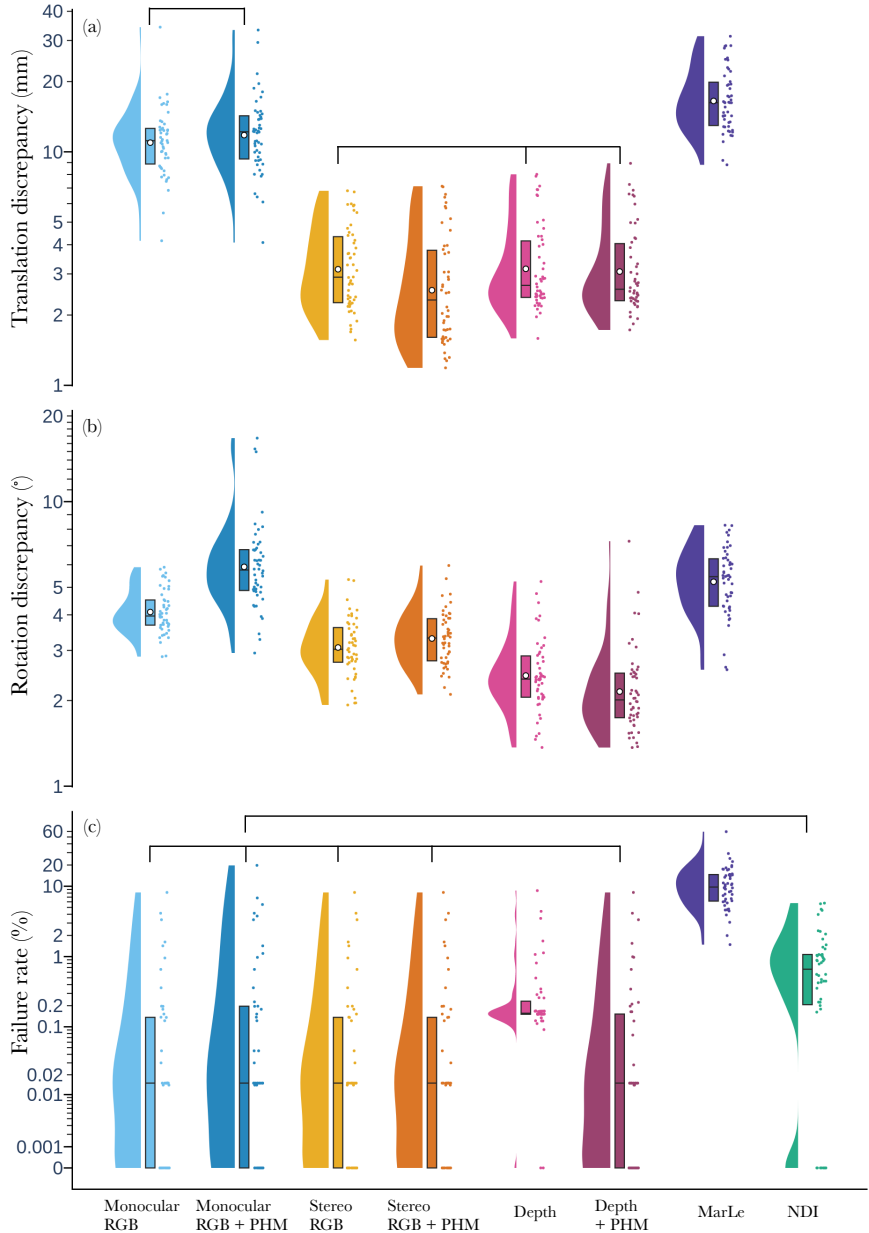


Figure 7: Performance of the head pose tracking methods evaluated empirically in 50 humans. Translation (a) and rotation (b) root-mean-square discrepancy (RMSD) of the proposed markerless methods as well as a re-implementation of a prior method, MarLe [31], relative to the conventional marker-based tracking system, NDI (see Figure 2 for summary). Failure rate (c) is given for all methods as a percentage of the total number of frames. Violin plots show the data distribution, dots mark the mean, and box plots denote the median surrounded by the interquartile range. The y-axes are log-spaced (before transformation, 0.001% was added to the data in (c) to accommodate zero values). All conditions were significantly different from each other at  $p < 0.05$  (with Holm multiple comparison correction) except for the groups denoted by brackets.

Tracking Method	Translation Discrepancy (mm)			Rotation Discrepancy (°)			Failure Rate (%)		
	Mean	Median	Interquartile Range	Mean	Median	Interquartile Range	Median	Interquartile Range	
Monocular RGB	10.952	11.160	3.727	4.094	3.965	0.829	<b>0.015</b>	<b>0.137</b>	
Monocular RGB + PHM	11.760	12.182	4.950	5.899	5.751	1.914	<b>0.015</b>	<b>0.197</b>	
Stereo RGB	3.141	2.904	2.073	3.071	3.030	0.883	<b>0.015</b>	<b>0.137</b>	
Stereo RGB + PHM	<b>2.555</b>	<b>2.319</b>	<b>2.184</b>	3.304	3.317	1.122	<b>0.015</b>	<b>0.137</b>	
Depth	3.155	2.679	1.777	2.448	2.379	0.817	0.157	0.085	
Depth + PHM	3.071	2.581	1.741	<b>2.150</b>	<b>2.011</b>	<b>0.755</b>	<b>0.015</b>	<b>0.153</b>	
MarLe	16.525	16.241	6.896	5.228	5.446	2.010	9.742	8.519	
NDI	—	—	—	—	—	—	0.672	0.866	

Table 1: Summary statistics of the head pose tracking methods’ performance data in Figure 7. Translation and rotation discrepancy statistics were calculated on the log-transformed data and back-transformed to the original units. Boldface indicates the best-performing method based on either the mean (for translation and rotation discrepancies) or the median (for failure rate).

$W_{350} = 0.961$ ,  $p < 0.0001$ ). A Friedman test also indicated that failure rate varied significantly across tracking methods ( $\chi^2_7 = 222$ ,  $p < 0.0001$ ; Kendall’s  $W = 0.634$ ). The grouped and ranked post-hoc test results are presented in Table 1, with detailed matrices compiled in Supplementary S.5.

Figure 7 visualizes the experimental performance of the individual tracking methods, with statistical significance of the differences assessed by the post-hoc t-tests with multiple comparison correction. The results highlight known limitations of monocular approaches for 3D localization, specifically the lack of direct depth measurement or stereoscopic triangulation, which hinders accurate distance estimation [58, 59]. When the statistically-regularized personalized head models (PHM) were not employed, stereo RGB performed similarly with the depth-based approach for spatial localization ( $p = 1.0000$ ), and an inferior angular localization performance against it ( $p = 0.0001$ ). The employment of PHM significantly improved the performance of stereo-based and depth-based tracking in different aspects, suggesting a complementary gain in tracking performance. With PHM, stereo-based tracking saw a 23% decrease in the mean of translation discrepancy ( $p < 0.0001$ ), but presented an 8% increase in its rotational counterpart ( $p < 0.0001$ ). Conversely, while the translation performance gain of the depth-based approach is statistically insignificant when employing PHM ( $p = 1.0000$ ), a 14% decrease in the mean of rotation discrepancy was observed ( $p = 0.029$ ). When comparing frame failure rates, stereo-RGB-camera-based and depth-sensor-based methodologies demonstrated an overall reduction in data loss compared to the NDI

system (except the Monocular RGB method  $p = 0.096$ ), which, in turn, outperformed MarLe ( $p < 0.0001$  against all other methods). The similar failure rate of multiple proposed methods suggests the limiting factor might be landmark detection, which can fail under large head displacement angles. These results also indicate that the robustness of the depth-based tracking method when employing PHM is comparable with RGB-based methods. The enhanced robustness, exemplified by the lower failure rate achieved by our proposed RGB and depth-based methods, can be explained by the NDI system’s reliance on the visibility of retroreflective markers, which can be occluded during natural head movements. In contrast, markerless methods leverage spatially distributed facial features with inherent redundancy, mitigating occlusion risks by eliminating the strict requirement for simultaneous visibility of all tracking points. Furthermore, the substantial reduction in data loss relative to the prior markerless method, MarLe, highlights the efficacy of the proposed algorithmic design, which demonstrates superior stability in maintaining valid pose estimation across a wider range of head orientations.

#### 4.2. Impact of Head Pose on Tracking

Figure 8 presents the tracking performance data as a function of parameters describing the head pose. Translational head movements introduced a slight increase in discrepancy relative to NDI across most proposed markerless tracking methods, with a generally gradual degradation. Rotational head movements, on the other hand, exerted more pronounced effects, particularly on RGB-based tracking performance. Both Monocular and Stereo RGB methods exhibited distinct “U-shaped” discrepancy curves, with tracking accuracy deteriorating sharply at the extremes of Yaw and Pitch. Conversely, depth-based methods tended to be more robust to rotational movements since they leverage a dense point cloud representation of the face.

## 5. Discussion

Compared to prior work on markerless neuronavigation [31], our study introduced advances in several key areas. First, we utilized MediaPipe’s 468 facial landmarks, which are denser and more accurate than the Dlib landmarks used previously [60]. Second, we employed higher-resolution cameras for all markerless algorithms, including our re-implementation of MarLe ( $3840 \times 2160$  compared to  $2048 \times 1536$ ,  $1920 \times 1080$ , and  $1280 \times 720$ ), thus

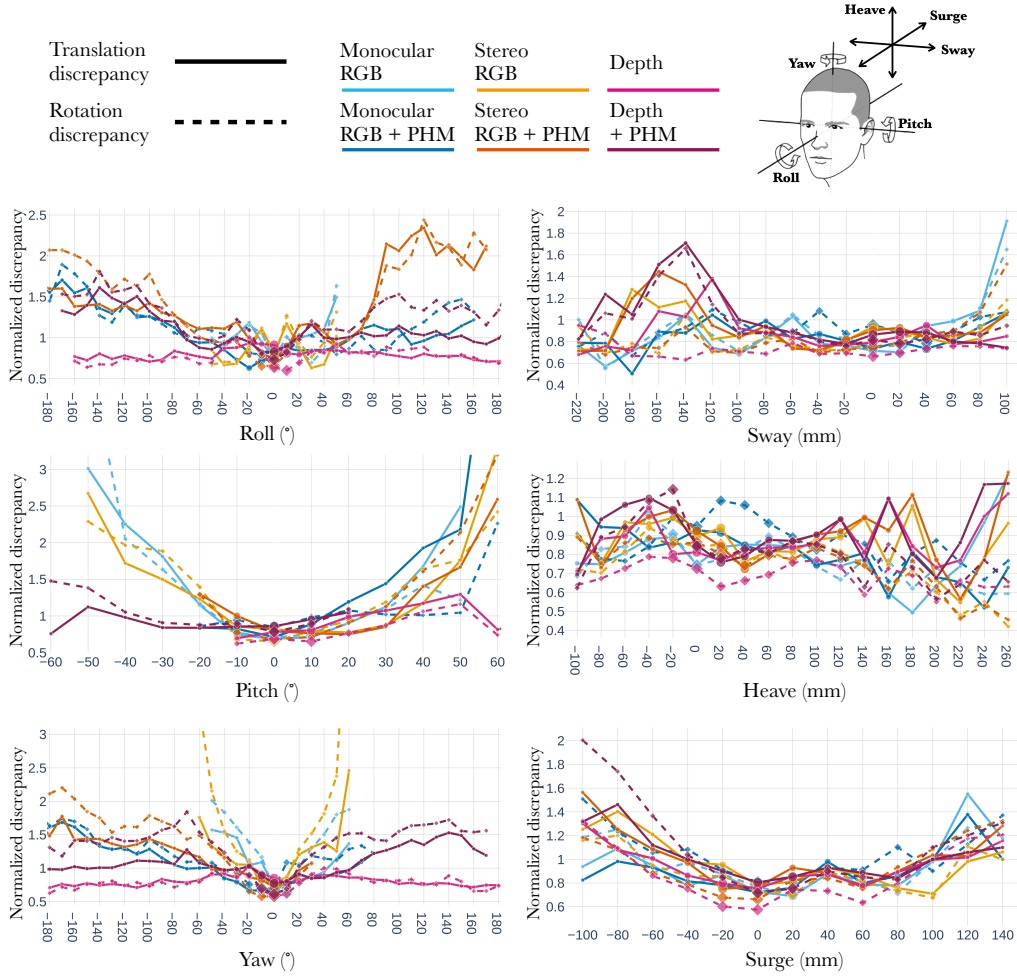


Figure 8: Mean translational and rotational tracking discrepancy as a function of the head pose parameters: sway, surge, heave, roll, pitch, and yaw. Each curve is normalized to its geometric mean value reported in Figure 7. The size of each scatter point is scaled proportionally to the data count.

enhancing facial geometry capture. Third, instead of using a single RGB input, our methods incorporated data from stereo RGB and time-of-flight depth sensors for richer 3D information. Fourth, we utilized advanced, individualized priors through the construction of personalized face and head models rather than generic anthropometric models, and showed the differences between the two options. Finally, we evaluated the spatiotemporal accuracy of 3D tracking in a diverse sample of 50 subjects, compared to a single subject in the prior work.

Our key finding is that head pose tracking methods that incorporate depth information, whether inferred via stereo pixel correspondence or measured directly by time-of-flight sensors, substantially outperform Monocular RGB-based techniques in both translational and angular accuracy, and they excel when subject-specific 3D priors (PHM) are employed. Interestingly, with such personalized head models based on statistical priors, we observed better translational accuracy improvement of the sparse, stereo-based method and better angular accuracy improvement of the dense, depth-based method. These findings suggest that accurate and robust markerless neuronavigation may benefit from multimodal approaches that combine the strengths of stereo RGB and depth sensors with personalized head models. Conversely, monocular RGB-based methods did not benefit from the use of personalized head models, likely due to the inherent limitations of monocular vision for 3D localization.

While this study utilized statistical priors fitted to camera-acquired facial geometry to construct the PHM, the proposed framework is compatible with subject-specific head models obtained via alternative modalities, including MRI, which is common in TMS research studies. The incorporation of ground-truth anatomical data would eliminate the need for shape estimation, thereby simplifying the workflow and potentially enhancing tracking accuracy by minimizing facial geometry approximation errors.

To contextualize the observed tracking performance within clinical requirements, it is instructive to consider the operational tolerances of TMS procedures. The dimensions of representative TMS targets are approximately 1–2 cm<sup>2</sup> [61, 62], while cortical target localization errors typically average between 4–8 mm [5]. Furthermore, while the NDI Polaris Vicra system used as the reference in this study has a volumetric accuracy of 0.25 mm with a 95% confidence interval of 0.5 mm [63], when accounting for registration errors, model inaccuracies, and tracker movement, standard marker-based TMS neuronavigation systems exhibit mean errors in the range of 5.0–5.7

mm, with a 95% confidence interval extending up to 11.5 mm [64, 65, 13]. Consequently, the tracking discrepancies between our markerless methods and the standard marker-based NDI system fall well within the error margins of the latter and the size of TMS targets, supporting the accuracy and effectiveness of our methods.

Limitations of this study include the following. (i) We relied on a relative accuracy assessment using a standard marker-based tracking system (NDI) as a reference, which itself has inherent accuracy limitations as detailed above. (ii) We focused on comparing the accuracy and proof of concept implementation of these three complementary modalities, but did not study the computational costs or real-time performance of these methods. Future work may explore the integration of these modalities into a single unified tracking approach that leverages the strengths of each method while balancing their computational demands. (iii) The proposed methods are implemented on a per-frame basis, and adding temporal consistency constraints is likely to further improve robustness and tracking accuracy.

Beyond performance, the proposed approaches help to lower the technological and financial barriers typically associated with neuronavigation. By utilizing affordable, consumer-grade sensors and adapting established computer vision techniques, the proposed methods offer an accessible alternative to conventional stereotactic systems, which require costly cameras and rigid tracker attachment. This affordability makes the system suitable for deployment in resource-limited settings, large-scale research studies where conventional neuronavigation may be impractical, and mobile applications.

## 6. Conclusions

Markerless head pose tracking using consumer-grade RGB-D sensor technology is feasible and can achieve localization accuracy suitable for TMS neuronavigation. Tracking methods that incorporate depth information and subject-specific head models significantly outperform monocular techniques in accuracy. These novel methods also improve upon the tracking failure rate compared to both markerless monocular approaches as well as the widely used marker-based stereotaxy, especially during extreme head pose deviations. There are opportunities to combine stereo RGB and depth sensor information with personalized statistical head models to enhance markerless tracking further. By eliminating the need for specialized camera hardware, physical marker attachment, and manual registration, the proposed marker-

less approach can substantially reduce setup complexity and cost. Overall, this work advances a new class of accessible, accurate, and non-invasive head tracking systems that leverage affordable, consumer-grade sensors and advanced modeling algorithms.

#### **Authorship contribution statement**

**Ziye Xie**: Methodology, Software, Investigation, Formal analysis, Writing – Original Draft, Visualization. **Oded Schlesinger**: Methodology, Software, Investigation, Formal analysis, Writing – Original Draft, Visualization. **Raj Kundu**: Methodology, Software, Investigation, Formal analysis, Writing – Original Draft, Visualization. **Jessica Y. Choi**: Investigation, Data Curation, Project administration. **Pablo Iturralde**: Writing – Review & Editing. **Dennis A. Turner**: Writing – Review & Editing. **Stefan M. Goetz**: Writing - Review & Editing. **Guillermo Sapiro**: Writing – Review & Editing, Supervision, Resources. **Angel V. Peterchev**: Conceptualization, Methodology, Writing – Review & Editing, Supervision, Resources, Project administration, Funding acquisition. **J. Matias Di Martino**: Conceptualization, Methodology, Writing – Review & Editing, Supervision, Resources, Project administration, Funding acquisition.

#### **Declaration of competing interest**

PI is a consultant for Dsene. SMG is inventor on patents and patent applications on transcranial magnetic stimulation (TMS) technology. Unrelated to this work, GS is also affiliated with Apple. AVP is inventor on patents and patent applications on TMS technology; has received patent royalties and consulting fees from Rogue Research; equity options, scientific advisory board membership, and consulting fees from Ampa Health; equity options, consulting fees, and travel support from Magnetic Tides; consulting fees from Soterix Medical; equipment loans from MagVenture; hardware donations from Magstim; and research funding from Motif. JMDM is a consultant for Restor3d, Pento, and Pyxis. The remaining authors declare that they do not have competing financial interests or personal relationships that could influence the work reported in this paper.

#### **Ethics statement**

This study followed ethical standards for research involving human subjects. The protocol was approved by the Duke University Health System Institutional Review Board (Protocol Pro00109130), and written informed

consent was obtained from all participants prior to data collection. To mitigate potential biases in computer vision facial recognition and tracking and provide robustness across diverse facial features and skin tones, the subject cohort included various races, ethnicities, sexes, and ages.

### **Acknowledgments**

For contributions to earlier stages of this project, we want to acknowledge Rohit Raguram, Ravitashaw Bathla, Zhuoqing Chang, Alexander Shang, Raymond Lin, and Dmitry Isaev. We also thank Dr. Joan Camprodon for advice on relevant clinical developments. Research reported in this publication was supported by a Germinator Award by the Duke Institute for Brain Sciences, the National Institute of Mental Health of the National Institutes of Health under Award Number R01MH129733, the Office of Naval Research Award Number N000142412211, the National Science Foundation Award Numbers DMS-2031849 and CCF-2120018, and the Simons Foundation Award Number 814643. Additional support from Apple Inc. is acknowledged. The content is solely the responsibility of the authors and does not necessarily represent the official views of the funding agencies.

## References

- [1] E. M. Wassermann, A. V. Peterchev, U. Ziemann, S. H. Lisanby, H. R. Siebner, V. Walsh, The Oxford Handbook of Transcranial Stimulation: Second Edition, Oxford University Press, 2024. doi:10.1093/oxfordhb/9780198832256.001.0001.  
URL <https://doi.org/10.1093/oxfordhb/9780198832256.001.0001>
- [2] C. L. Scrivener, A. T. Reader, Variability of eeg electrode positions and their underlying brain regions: visualizing gel artifacts from a simultaneous eeg-fmri dataset, *Brain and Behavior* 12 (2) (2022) e2476.
- [3] K. Cleary, T. M. Peters, Image-guided interventions: technology review and clinical applications, *Annual Review of Biomedical Engineering* 12 (1) (2010) 119–142.
- [4] A. Karataş, A. Erdem, A. Savaş, G. Kutlu, B. Yağmurlu, I. Erden, E. Bilir, Identification and removal of an epileptogenic lesion using ictal-eeg, functional-neuronavigation and electrocorticography, *Journal of Clinical Neuroscience* 11 (3) (2004) 343–346.
- [5] J.-P. Lefaucheur, T. Picht, The value of preoperative functional cortical mapping using navigated tms, *Neurophysiologie Clinique/Clinical Neurophysiology* 46 (2) (2016) 125–133.
- [6] S. F. W. Neggers, T. R. Langerak, D. J. L. G. Schutter, R. C. W. Mandl, N. F. Ramsey, P. J. J. Lemmens, A. Postma, A stereotactic method for image-guided transcranial magnetic stimulation validated with fMRI and motor-evoked potentials, *NeuroImage* 21 (4) (2004) 1805–1817. doi:10.1016/j.neuroimage.2003.12.006.  
URL <https://www.sciencedirect.com/science/article/pii/S1053811903007602>
- [7] C. Schönfeldt-Lecuona, A. Thielscher, R. W. Freudenmann, M. Kron, M. Spitzer, U. Herwig, Accuracy of stereotaxic positioning of transcranial magnetic stimulation, *Brain Topography* 17 (4) (2005) 253–259. doi:10.1007/s10548-005-6033-1.

[8] E. M. Wassermann, A. V. Peterchev, U. Ziemann, S. H. Lisanby, H. R. Siebner, V. Walsh, The oxford handbook of transcranial stimulation: second edition, Oxford University Press, 2024. doi:10.1093/oxfordhb/9780198832256.001.0001.  
URL <https://doi.org/10.1093/oxfordhb/9780198832256.001.0001>

[9] M. Ivanov, A. Vlad Ciurea, Neuronavigation. principles. surgical technique., *Journal of Medicine and Life* 2 (1) (2009) 29–35.  
URL <https://www.ncbi.nlm.nih.gov/pmc/articles/PMC5051478/>

[10] R. J. Maciunas, R. L. Galloway Jr, J. W. Latimer, The application accuracy of stereotactic frames, *Neurosurgery* 35 (4) (1994) 682–695.

[11] K. L. Holloway, S. E. Gaede, P. A. Starr, J. M. Rosenow, V. Ramakrishnan, J. M. Henderson, Frameless stereotaxy using bone fiducial markers for deep brain stimulation, *Journal of Neurosurgery* 103 (3) (2005) 404–413.

[12] C. R. Maurer, J. M. Fitzpatrick, M. Y. Wang, R. L. Galloway, R. J. Maciunas, G. S. Allen, Registration of head volume images using implantable fiducial markers, *IEEE Transactions on Medical Imaging* 16 (4) (1997) 447–462.

[13] A. E. Nieminen, J. O. Nieminen, M. Stenroos, P. Novikov, M. Nazarova, S. Vaalto, V. Nikulin, R. J. Ilmoniemi, Accuracy and precision of navigated transcranial magnetic stimulation, *Journal of Neural Engineering* 19 (6) (2022) 066037.

[14] T. Mitsui, M. Fujii, M. Tsuzaka, Y. Hayashi, Y. Asahina, T. Wakabayashi, Skin shift and its effect on navigation accuracy in image-guided neurosurgery, *Radiological Physics and Technology* 4 (1) (2011) 37–42.

[15] S. M. Goetz, I. C. Kozyrkov, B. Luber, S. H. Lisanby, D. L. K. Murphy, W. M. Grill, A. V. Peterchev, Accuracy of robotic coil positioning during transcranial magnetic stimulation, *Journal of Neural Engineering* 16 (5) (2019) 054003. doi:10.1088/1741-2552/ab2953.

[16] A. Barton, D. Broadhurst, J. Hitchcock, C. Lund, L. McNichol, C. R. Ratliff, J. T. Moraes, S. Yates, M. Gray, *Medical Adhesive-*

Related Skin Injury at 10 Years: An Updated Consensus, *Journal of Wound Ostomy & Continence Nursing* 51 (5S) (2024) S2. doi:10.1097/WON.0000000000001116.  
URL [https://journals.lww.com/jwocnonline/fulltext/2024/09001/medical\\_adhesive\\_related\\_skin\\_injury\\_at\\_10\\_years\\_.2.aspx](https://journals.lww.com/jwocnonline/fulltext/2024/09001/medical_adhesive_related_skin_injury_at_10_years_.2.aspx)

- [17] N. J. Thornton, B. R. Gibson, A. M. Ferry, B. Gibson, Contact dermatitis and medical adhesives: a review, *Cureus* 13 (3) (2021).
- [18] J. M. Houck, E. D. Claus, A comparison of automated and manual co-registration for magnetoencephalography, *PLOS One* 15 (4) (2020) e0232100.
- [19] I. Chiurillo, R. M. Sha, F. C. Robertson, J. Liu, J. Li, H. Le Mau, J. M. Amich, W. B. Gormley, R. Stolyarov, High-accuracy neuro-navigation with computer vision for frameless registration and real-time tracking, *Bioengineering* 10 (12) (2023) 1401.
- [20] F. V. Kögl, É. Léger, N. Haouchine, E. Torio, P. Juvekar, N. Navab, T. Kapur, S. Pieper, A. Golby, S. Frisken, A tool-free neuronavigation method based on single-view hand tracking, *Computer Methods in Biomechanics and Biomedical Engineering: Imaging & Visualization* 11 (4) (2023) 1307–1315.
- [21] C. Gsaxner, A. Pepe, J. Wallner, D. Schmalstieg, J. Egger, Markerless image-to-face registration for untethered augmented reality in head and neck surgery, in: *International Conference on Medical Image Computing and Computer-Assisted Intervention*, Springer, 2019, pp. 236–244.
- [22] S. Sathyanarayana, C. Leuze, B. Hargreaves, B. Daniel, G. Wetzstein, A. Etkin, M. T. Bhati, J. A. McNab, Comparison of head pose tracking methods for mixed-reality neuronavigation for transcranial magnetic stimulation, in: *Medical Imaging 2020: Image-Guided Procedures, Robotic Interventions, and Modeling*, Vol. 11315, SPIE, 2020, pp. 147–154.
- [23] F. Manni, A. Elmi-Terander, G. Burström, O. Persson, E. Edström, R. Holthuizen, C. Shan, S. Zinger, F. van der Sommen, P. H. de With,

Towards optical imaging for spine tracking without markers in navigated spine surgery, *Sensors* 20 (13) (2020) 3641.

- [24] Y. Liu, Z. Song, M. Wang, A new robust markerless method for automatic image-to-patient registration in image-guided neurosurgery system, *Computer Assisted Surgery* 22 (sup1) (2017) 319–325.
- [25] T. Zeng, Y. Lu, W. Jiang, J. Zheng, J. Zhang, P. Gravel, Q. Wan, K. Fontaine, T. Mulnix, Y. Jiang, et al., Markerless head motion tracking and event-by-event correction in brain pet, *Physics in Medicine & Biology* 68 (24) (2023) 245019.
- [26] Y. Huang, O. Taheri, M. J. Black, D. Tzionas, Intercap: joint markerless 3d tracking of humans and objects in interaction from multi-view rgb-d images, *International Journal of Computer Vision* 132 (7) (2024) 2551–2566.
- [27] H. Cuevas-Velasquez, A. Yiannakidis, S. Shin, G. Becherini, M. Höschle, J. Tesch, T. Obersat, T. Alexiadis, M. Black, Mamma: Markerless & automatic multi-person motion action capture, *arXiv preprint arXiv:2506.13040* (2025).
- [28] C. Brambilla, R. Marani, L. Romeo, M. L. Nicora, F. A. Storm, G. Reni, M. Malosio, T. D’Orazio, A. Scano, Azure kinect performance evaluation for human motion and upper limb biomechanical analysis, *Heliyon* 9 (11) (2023).
- [29] J. Bertram, T. Krüger, H. M. Röhling, A. Jelusic, S. Mansow-Model, R. Schniepp, M. Wuehr, K. Otte, Accuracy and repeatability of the microsoft azure kinect for clinical measurement of motor function, *PLOS One* 18 (1) (2023) e0279697.
- [30] M. Villa, J. Sancho, G. Rosa-Olmeda, M. Chavarrias, E. Juarez, C. Sanz, Benchmarking commercial depth sensors for intraoperative markerless registration in neurosurgery applications, *International Journal of Computer Assisted Radiology and Surgery* (2025).
- [31] R. H. Matsuda, V. H. Souza, P. N. Kirsten, R. J. Ilmoniemi, O. Baffa, Marle: Markerless estimation of head pose for navigated transcranial magnetic stimulation, *Physical and Engineering Sciences in Medicine* (2023) 1–10.

[32] S. Ploumpis, E. Ververas, E. O’Sullivan, S. Moschoglou, H. Wang, N. Pears, W. A. Smith, B. Gecer, S. Zafeiriou, Towards a complete 3d morphable model of the human head, *IEEE Transactions on Pattern Analysis and Machine Intelligence* 43 (11) (2020) 4142–4160.

[33] R. I. Hartley, A. Zisserman, *Multiple view geometry in computer vision*, 2nd Edition, Cambridge University Press, ISBN: 0521540518, 2004.

[34] K. Madsen, H. B. Nielsen, O. Tingleff, *Methods for non-linear least squares problems* (2004).

[35] D. F. Dementhon, L. S. Davis, Model-based object pose in 25 lines of code, *International Journal of Computer Vision* 15 (1) (1995) 123–141, company: Springer Distributor: Springer Institution: Springer Label: Springer Number: 1 Publisher: Kluwer Academic Publishers. doi:10.1007/BF01450852.  
URL <https://link.springer.com/article/10.1007/BF01450852>

[36] B. M. Haralick, C.-N. Lee, K. Ottenberg, M. Nölle, Review and analysis of solutions of the three point perspective pose estimation problem, *International Journal of Computer Vision* 13 (3) (1994) 331–356. doi:10.1007/BF02028352.  
URL <https://doi.org/10.1007/BF02028352>

[37] V. Lepetit, F. Moreno-Noguer, P. Fua, Epnp: An accurate  $O(n)$  solution to the pnp problem, *International Journal of Computer Vision* 81 (2) (2009) 155–166. doi:10.1007/s11263-008-0152-6.  
URL <https://doi.org/10.1007/s11263-008-0152-6>

[38] Y. Kartynnik, A. Ablavatski, I. Grishchenko, M. Grundmann, Real-time facial surface geometry from monocular video on mobile gpus, arXiv:1907.06724 [cs] (Jul. 2019). doi:10.48550/arXiv.1907.06724.  
URL <http://arxiv.org/abs/1907.06724>

[39] Z. Liu, X. Zhu, G. Hu, H. Guo, M. Tang, Z. Lei, N. M. Robertson, J. Wang, Semantic alignment: Finding semantically consistent ground-truth for facial landmark detection, in: *Proceedings of the IEEE/CVF conference on computer vision and pattern recognition*, 2019, pp. 3467–3476.

[40] Microsoft azure kinect sdk, (Retrieved on October 6, 2025) (2022).  
 URL <https://github.com/microsoft/Azure-Kinect-Sensor-SDK>

[41] P. J. Besl, N. D. McKay, Method for registration of 3-d shapes, in: Sensor fusion IV: Control Paradigms and Data Structures, Vol. 1611, Spie, 1992, pp. 586–606.

[42] J. Booth, A. Roussos, S. Zafeiriou, A. Ponniah, D. Dunaway, A 3d morphable model learnt from 10,000 faces, in: Proceedings of the IEEE Conference on Computer Vision and Pattern Recognition, 2016, pp. 5543–5552.

[43] O. Schlesinger, R. Kundu, D. Isaev, J. Y. Choi, S. M. Goetz, D. A. Turner, G. Sapiro, A. V. Peterchev, J. M. Di Martino, Scalp surface estimation and head registration using sparse sampling and 3d statistical models, *Computers in Biology and Medicine* 178 (2024) 108689.

[44] O. Schlesinger, R. Kundu, S. Goetz, G. Sapiro, A. V. Peterchev, J. M. Di Martino, Automatic neurocranial landmarks detection from visible facial landmarks leveraging 3d head priors, in: *Workshop on Clinical Image-Based Procedures*, Springer, 2023, pp. 12–20.

[45] H. Dai, N. Pears, W. A. Smith, C. Duncan, A 3d morphable model of craniofacial shape and texture variation, in: Proceedings of the IEEE International Conference on Computer Vision, 2017, pp. 3085–3093.

[46] S. Ploumpis, H. Wang, N. Pears, W. A. Smith, S. Zafeiriou, Combining 3d morphable models: A large scale face-and-head model, in: Proceedings of the IEEE/CVF Conference on Computer Vision and Pattern Recognition, 2019, pp. 10934–10943.

[47] R. Gross, I. Matthews, J. Cohn, T. Kanade, S. Baker, Multi-pie, *Image and Vision Computing* 28 (5) (2010) 807–813.

[48] H. H. Jasper, The ten-twenty electrode system of the international federation, *Electroencephalography and Clinical Neurophysiology* 10 (1958) 370–375.

[49] J. Green, R. Kundu, A. V. Peterchev, J. M. D. Martino, Toward Accessible Neuronavigation: Tracking Retroreflective Markers with a Consumer-Grade Depth Camera, in: *2024 IEEE URUCON*, 2024, pp.

1–5. doi:10.1109/URUCON63440.2024.10850257.  
URL <https://ieeexplore.ieee.org/document/10850257>

- [50] X. Zhu, D. Ramanan, Face detection, pose estimation, and landmark localization in the wild, in: 2012 IEEE conference on computer vision and pattern recognition, IEEE, 2012, pp. 2879–2886.
- [51] C. Ding, D. Tao, A comprehensive survey on pose-invariant face recognition, ACM Transactions on intelligent systems and technology (TIST) 7 (3) (2016) 1–42.
- [52] G. Van Rossum, F. L. Drake, et al., Python reference manual, Vol. 111, Centrum voor Wiskunde en Informatica Amsterdam, 1995, version 3.10.12.
- [53] R. C. Team, et al., R: A language and environment for statistical computing, R foundation for statistical computing, Vienna, AustriaVersion 4.5.2 (2021).
- [54] L. Gautier, rpy2: Python interface to the R language, version 3.6.4 (Retrieved on April 4, 2024) (2024).  
URL <https://rpy2.github.io/>
- [55] R. Vallat, Pingouin: statistics in Python., J. Open Source Softw. 3 (31) (2018) 1026.
- [56] S. Seabold, J. Perktold, et al., Statsmodels: econometric and statistical modeling with Python., SciPy 7 (1) (2010) 92–96.
- [57] P. Virtanen, R. Gommers, T. E. Oliphant, M. Haberland, T. Reddy, D. Cournapeau, E. Burovski, P. Peterson, W. Weckesser, J. Bright, et al., Scipy 1.0: fundamental algorithms for scientific computing in Python, Nature methods 17 (3) (2020) 261–272.
- [58] J. Zhang, Survey on monocular metric depth estimation, arXiv preprint arXiv:2501.11841 (2025).
- [59] Y. Guo, T. Gao, A. Dong, X. Jiang, Z. Zhu, F. Wang, A survey of the state of the art in monocular 3d human pose estimation: Methods, benchmarks, and challenges, Sensors (Basel, Switzerland) 25 (8) (2025) 2409.

- [60] R. Chandel, R. Bhowmick, U. Hariharan, A comparison of face landmark detection techniques, in: 2023 4th International Conference on Computation, Automation and Knowledge Management (ICCAKM), IEEE, 2023, pp. 1–6.
- [61] L. M. Koponen, J. O. Nieminen, R. J. Ilmoniemi, Multi-locus transcranial magnetic stimulation—theory and implementation, *Brain Stimulation* 11 (4) (2018) 849–855.
- [62] A. Giuffre, C. K. Kahl, E. Zewdie, J. G. Wrightson, A. Bourgeois, E. G. Condilffe, A. Kirton, Reliability of robotic transcranial magnetic stimulation motor mapping, *Journal of Neurophysiology* (2021).
- [63] Northern Digital, Inc., Polaris vicra, compact optical tracker for small oem instruments, <https://www.ndigital.com/optical-navigation-technology/polaris-vicra/>, (Retrieved on October 22, 2024) (2024).
- [64] J. Ruohonen, J. Karhu, Navigated transcranial magnetic stimulation, *Neurophysiologie clinique/Clinical neurophysiology* 40 (1) (2010) 7–17.
- [65] I. Soterix Medical, Neural navigator, k191422, (Retrieved on April 4, 2024) (2020).  
URL [https://www.accessdata.fda.gov/cdrh\\_docs/pdf19/K191422.pdf](https://www.accessdata.fda.gov/cdrh_docs/pdf19/K191422.pdf)
- [66] Ndi combined api c interface library, (Retrieved on October 6, 2025) (2023).  
URL <https://github.com/PlusToolkit/ndicapi>
- [67] libjpeg-turbo, (Retrieved on August 14, 2025) (2025).  
URL <https://libjpeg-turbo.org/>
- [68] Dear imgui, (Retrieved on August 14, 2025) (2025).  
URL <https://github.com/ocornut/imgui>
- [69] W. Schroeder, K. Martin, B. Lorensen, *The Visualization Toolkit* (4th ed.), Kitware, 2006.
- [70] imgui-vtk, (Retrieved on October 6, 2025) (2023).  
URL <https://github.com/trlsmax/imgui-vtk>

- [71] B. Shoshany, A c++ 17 thread pool for high-performance scientific computing, *SoftwareX* 26 (2024) 101687.
- [72] Spscqueue, (Retrieved on August 14, 2025) (2023).  
URL <https://github.com/rigtorp/SPSCQueue>
- [73] G. Bradski, The OpenCV Library, *Dr. Dobb's Journal of Software Tools* (2000).
- [74] S. Choi, Q.-Y. Zhou, V. Koltun, Robust reconstruction of indoor scenes, in: *Proceedings of the IEEE Conference on Computer Vision and Pattern Recognition*, 2015, pp. 5556–5565.
- [75] H. G. Barrow, J. M. Tenenbaum, R. C. Bolles, H. C. Wolf, Parametric correspondence and chamfer matching: Two new techniques for image matching, in: *Proceedings: Image Understanding Workshop*, Science Applications, Inc, 1977, pp. 21–27.

## Appendix A. Supplementary Materials

### *S.1. Experimental Setup*

#### *S.1.1. Acquisition Hardware*

Reference data were obtained using the NDI Polaris Vicra optical measurement system. This stereotaxy camera system utilizes infrared light to detect a set of retroreflective markers attached to the subject’s head. Experimental data were captured using two Microsoft Azure Kinect DK devices running in Master and Subordinate mode. Each Azure device records both RGB and infrared/depth data simultaneously, at 30 frames per second (FPS) in both domains and with respective resolutions of  $3840 \times 2160$  and  $640 \times 576$  pixels.

Both Azure Kinect DK devices were mounted on a 3.18 mm-thick aluminum L-channel, oriented coplanarly but offset horizontally by 355 mm. The NDI Polaris Vicra was also mounted to this system to ensure all collected 3D data were rigidly related (see Figure 1). All data collection devices were connected to USB 3.0+ controllers on a Dell XPS 8950 desktop computer (i7-12700 @ 2.1-4.9 GHz, 32 GB RAM, RTX 3090 GPU).

#### *S.1.2. Acquisition Software*

Real-time dataset acquisition was achieved using a custom multi-threaded C++ application. The Microsoft Azure Kinect SDK was used to interface with the Azure Kinect DK devices. The NDI Combined API C Interface Library [66] was used to interface with the NDI Polaris Vicra. The libjpeg-turbo library [67] was used to decode RGB data, which was natively transmitted in MJPEG format by the Azure Kinect DK devices. Data captured by the Azure Kinect DK devices was written to disk by the Azure Kinect SDK in Matroska Multimedia Container format. Data captured by the NDI Polaris Vicra was reported as homogeneous  $4 \times 4$  transformation matrices (1 matrix per tracker per time point) and written to disk in plain text format.

The application was primarily designed using the Dear ImGui library [68] to enable real-time visualization. The Visualization Toolkit (VTK) library [69] was used for real-time rendering of 3D data. Integration of the VTK and Dear ImGui libraries was achieved using a forked version of the imgui-vtk library [70].

Real-time data capture was coordinated using a thread pool, implemented using the BS::thread\_pool library [71]. Under this paradigm, data from both Azure Kinect DK devices was concurrently processed in separate threads,

added to a queue, and visualized by the application’s main thread. In this way, inter-thread communication was implemented with multiple single-producer, single-consumer queues and the SPSCQueue library [72]. Overall, the design of the custom C++ application allowed for data capture as well as real-time visualization.

### *S.1.3. Camera Calibration*

Camera calibration was achieved using a custom, OpenCV-based [73] pipeline as follows. A  $9 \times 13$  chessboard pattern (square edge is 25.4 mm long) was printed on a 5 mm thick foam board. Intrinsic and extrinsic calibration data for both cameras were then acquired simultaneously by moving the chessboard poster in various positions and orientations throughout the fields of view of both cameras. Both Azure Kinect DK devices were configured to record RGB data synchronously at  $3840 \times 2160$  resolution and 30 FPS with an exposure time of 2.5 ms per frame. IR data was captured in passive IR mode (i.e., with the time-of-flight emitter disabled) at  $1024 \times 1024$  resolution and 30 FPS with a 1.6 ms exposure time. Ambient illumination was increased with artificial lighting to maintain proper image exposure. Inter-device synchronization was achieved using the manufacturer’s firmware via a wired connection.

First, intrinsic parameters were estimated for each camera using only those video frames for which the chessboard was in view of the individual camera (OpenCV `findChessboardCorners` function [73]). Second, stereo calibration was performed (OpenCV `stereoCalibrate` function) using only those pairs of frames for which the chessboard was detected in both cameras. Frame pairs were synchronized across Azure Kinect DK devices using hardware-based synchronization data. As the original recordings were at 30 FPS (i.e., consecutive frames have high correlation), we split the data into 10 datasets equivalent to a 3 FPS recording (taking 1 every ten frames). Effectively, 10 intrinsic calibrations were performed for each camera, and the final camera matrix and distortion coefficients were obtained by element-wise averaging the output of the 10 trials. Similarly, after synchronization, the stereo calibration dataset was split into 10 smaller datasets, and the calibration matrices were obtained by element-wise averaging of the output of the 10 trials.

### *S.2. Study Participants Composition*

The demographic composition of the study subjects is summarized in Table S.1.

Gender (# subj)		Age (years)			Race (%)				Ethnicity (%)		
Female	Male	Min	Mean	Max	White	Black or African American	Asian	More than one race	American Indian or Alaska Native	Hispanic or Latino	Not Hispanic or Latino
27	23	20	28.6	76	38	30	26	4	2	26	74

Table S.1: Demographic composition of study subjects. Participants were volunteers from the general population.

### S.3. Design Choice Analysis for RGB-based Tracking Methods

#### S.3.1. Facial Landmark Selection

The use of RGB-based methods in Section 3.1.2 and Section 3.1.3 relies on facial landmarks. Hence, it is critical to determine which facial landmarks could be used for accurate subject head tracking. Salient facial areas, including eyebrows, eyes, nose, and mouth, were empirically observed to have a higher detection accuracy over significant head movements. We used facial landmarks that cover the lower part of the eyes and the nose as the base subset of the facial landmarks, and compared the tracking accuracy of the RGB-based methods between them and when additional facial landmarks, such as those covering the nose or the mouth, are involved. Specifically, four subsets of the total detected facial landmarks were selected: areas cover the lower part of the eyes and the nose, areas cover the lower part of the eyes, the nose and the eyebrows, areas cover the lower part of the eyes, the nose and the mouth, and areas cover the lower part of the eyes, the nose, the eyebrows and the mouth. When the PHM was used as the 3D head model, a sparse subset of these detected landmarks that is Multi-PIE compatible was used. A visualization of the set of landmarks tested is shown in Figure S.1, and tracking accuracy is provided in Tables S.2 and S.3.

### S.4. Subject Representations

#### S.4.1. Three-Dimensional Morphable Models

Three-dimensional morphable models (3DMMs) are statistical models that capture object class variability. They are typically constructed by acquiring and aligning numerous 3D object scans. A 3DMM is characterized by its mean shape,  $S_{mean}$ , and a set of  $K$  principal component vectors, denoted  $\mathbf{v} = [v_1 \dots v_k]$ ,  $v_i \in \mathbb{R}^n$ , and their corresponding eigenvalues,  $\mathbf{e} = [e_1 \dots e_k]$ , obtained through principal component analysis (PCA). These components represent the dominant modes of shape variation, maintaining dense correspondence with the mean shape. New object instances,  $S_w$ , can be generated

Monocular RGB-based Tracking		Euclidean Distance RMSD (mm)		
Landmark Areas		Median	Mean	SD
	Eyes + Nose (Figure S.1a)	12.345	12.838	4.012
	Eyes + Nose + Eyebrows (Figure S.1b)	11.707	12.045	3.559
	Eyes + Nose + Mouth (Figure S.1c)	12.380	12.897	4.831
	Eyes + Nose + Eyebrows + Mouth (Figure S.1d)	11.160	11.582	4.403
	* Eyes + Nose (Figure S.1e)	12.580	13.011	4.024
	* Eyes + Nose + Eyebrows (Figure S.1f)	11.572	11.916	3.496
	* Eyes + Nose + Mouth (Figure S.1g)	12.788	13.373	5.080
	* Eyes + Nose + Eyebrows + Mouth (Figure S.1h)	11.118	11.689	4.164
PHM	* Eyes + Nose (Figure S.1e)	18.922	19.065	5.107
	* Eyes + Nose + Eyebrows (Figure S.1f)	14.324	14.675	4.652
	* Eyes + Nose + Mouth (Figure S.1g)	15.448	15.707	5.234
	* Eyes + Nose + Eyebrows + Mouth (Figure S.1h)	12.182	12.667	5.258

Table S.2: Tracking accuracy results of the Monocular RGB tracking with different facial landmark subsets. Median, mean, and standard deviation (SD) of Euclidean RMSD are reported. Subsets beginning with a star (\*) indicate the sparse subset of landmarks that approximates the Dlib landmark configuration.

Stereo RGB-based Tracking		Euclidean Distance RMSD (mm)		
Landmark Areas		Median	Mean	SD
	Eyes + Nose (Figure S.1a)	3.581	4.052	1.318
	Eyes + Nose + Eyebrows (Figure S.1b)	3.454	3.947	1.389
	Eyes + Nose + Mouth (Figure S.1c)	3.022	3.491	1.414
	Eyes + Nose + Eyebrows + Mouth (Figure S.1d)	2.904	3.410	1.444
	* Eyes + Nose (Figure S.1e)	3.454	3.956	1.330
	* Eyes + Nose + Eyebrows (Figure S.1f)	3.411	3.881	1.405
	* Eyes + Nose + Mouth (Figure S.1g)	2.989	3.503	1.415
	* Eyes + Nose + Eyebrows + Mouth (Figure S.1h)	2.894	3.444	1.446
PHM	* Eyes + Nose (Figure S.1e)	2.417	3.089	1.699
	* Eyes + Nose + Eyebrows (Figure S.1f)	2.438	3.078	1.712
	* Eyes + Nose + Mouth (Figure S.1g)	2.421	3.049	1.706
	* Eyes + Nose + Eyebrows + Mouth (Figure S.1h)	2.325	2.955	1.722

Table S.3: Tracking accuracy results of the Stereo RGB tracking method for different facial landmark subsets. Median, mean, and SD of Euclidean RMSD are reported. Subsets beginning with a star (\*) indicate the sparse subset of landmarks that approximates the Dlib landmark configuration.

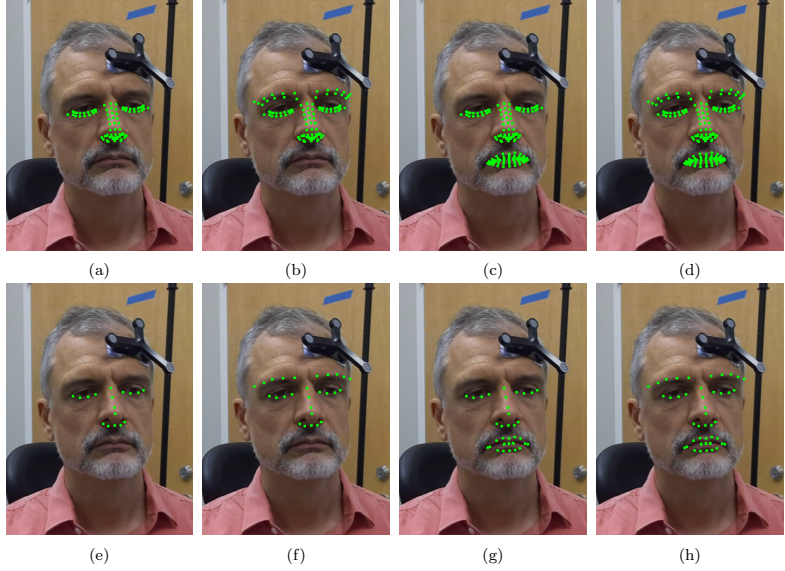


Figure S.1: Visualization of the eight facial landmark combinations with dense landmarks on top and the Multi-PIE compatible sparse versions on the bottom. (a) Selected lower eye and nose area landmarks; (b) Selected lower eye, nose and eyebrows area landmarks; (c) Selected lower eye, nose and mouth area landmarks; (d) A union set of (a), (b) and (c); (e) Sparse version of (a), Multi-PIE-compatible; (f) Sparse version of (b), Multi-PIE-compatible; (g) Sparse version of (c), Multi-PIE-compatible, and (h) A union set of (e), (f) and (g).

by linearly combining the mean shape with a weighted sum,  $w$ , of the eigenvalues multiplied by eigenvectors with customized weights:

$$w = [w_1 \dots w_k], w_i \in \mathbb{R}, \quad (\text{S.1})$$

$$S_w = S_{mean} + \sum_{i=1}^k w_i \cdot e_i \cdot v_i. \quad (\text{S.2})$$

This structure allows for a comprehensive yet efficient representation of object instances by retaining only the most significant variations, thereby substantially reducing the parameter space.

#### S.4.2. 3DMM Fitting Procedure

The modeling procedure begins with the selection of a subset of consecutive frames from the depth sensor face scan recording, followed by the detection of facial landmarks within these frames. These frames are not part

of any future tracking steps. Let  $\mathcal{N} = n_1, n_2, \dots, n_N$  represent the set of selected frames. For each frame  $n_k \in \mathcal{N}$ , the detected 2D facial landmarks from the left Azure RGB images are denoted as  $\mathbf{p}^L[n] = p_i^L[n]_{i=1}^{468}$ , as described in Section 3.1.2. Using the extracted convex hull from  $\mathbf{p}^L[n_k]$ , the corresponding depth data is masked to obtain the dense facial point clouds. Let  $\mathbf{D}_{face}^L[n_k]$  represent the segmented 3D facial point clouds from the left Azure device at frame  $n_k$ . To capture the subject-specific 3D facial geometry, the full set of selected point clouds is aggregated:

$$\mathbf{D}_{face} = \bigcup_{\mathcal{N}} (\mathbf{D}_{face}^L[n_k]). \quad (\text{S.3})$$

These point clouds are subsequently aligned using a multi-way registration method [74] to produce an aggregated and downsampled point cloud, denoted as  $\mathcal{X}_{face}$ . This point cloud serves as a representation of the subject’s facial geometry captured by the Azure system.

Subsequently, an optimization framework inspired by Schlesinger et al. [43] was employed to deform the 3DMM template to fit the aggregated point cloud,  $\mathcal{X}_{face}$ , derived from Azure-captured point clouds as described in Section 3.1.4. This process involves computing a set of weights to fit the 3DMM to the subject face geometry,  $w$ , and computing the transformation that aligns both point clouds,  $T$ . This optimization, capturing the unique facial geometry and yielding the subject-specific model, can be formulated as the minimization of the objective function provided in Equation (S.4)

$$l(w, T) = d_{\text{Chamfer}}(\mathcal{X}_{face}, \mathcal{X}_{UHM}) + \lambda (\|w\|_F + \|T - T_0\|_F), \quad (\text{S.4})$$

where  $d_{\text{Chamfer}}$  quantifies the geometric discrepancy between two point clouds by measuring the average distances between corresponding points and the angles between their respective surface normals, as defined by the Chamfer distance metric [75]; the second term acts as a regularization factor penalizing high deformations or transformations.

#### S.4.3. Rigid Alignment of Face and Head Models

Since the 3D facial and head models used in this study have different coordinate systems, e.g., origins for each PHM are at the nasion, and their counterpart for the MediaPipe Face Model (MP) is the center of their internal head model [38], it is necessary to ensure that all tracking methods report transformations towards the same coordinate frame. We selected the

coordinate frame of the PHM as the common coordinate frame of the head, and estimated the rigid transformation to map to this reference frame from other models when needed.

### S.5. Statistical Analysis Post-Hoc Pairwise Comparison P-Values

Tracking Method	Monocular RGB	Monocular RGB + PHM	Stereo RGB	Stereo RGB + PHM	Depth	Depth + PHM	MarLe
Monocular RGB	—						
Monocular RGB + PHM	0.0801	—					
Stereo RGB	<0.0001	<0.0001	—				
Stereo RGB + PHM	<0.0001	<0.0001	<0.0001	—			
Depth	<0.0001	<0.0001	1.0000	<0.0001	—		
Depth + PHM	<0.0001	<0.0001	1.0000	0.0004	1.0000	—	
MarLe	<0.0001	<0.0001	<0.0001	<0.0001	<0.0001	<0.0001	—

Table S.4: Post-hoc pairwise comparisons for translation discrepancy ( $p$ -values), corresponding to tracking method ranking in Table 1.

Tracking Method	Monocular RGB	Monocular RGB + PHM	Stereo RGB	Stereo RGB + PHM	Depth	Depth + PHM	MarLe
Monocular RGB	—						
Monocular RGB + PHM	<0.0001	—					
Stereo RGB	<0.0001	<0.0001	—				
Stereo RGB + PHM	<0.0001	<0.0001	<0.0001	—			
Depth	<0.0001	<0.0001	0.0001	<0.0001	—		
Depth + PHM	<0.0001	<0.0001	<0.0001	<0.0001	0.0289	—	
MarLe	<0.0001	0.0326	<0.0001	<0.0001	<0.0001	<0.0001	—

Table S.5: Post-hoc pairwise comparisons for rotation discrepancy ( $p$ -values), corresponding to tracking method ranking in Table 1.

Tracking Method	Monocular RGB	Monocular RGB + PHM	Stereo RGB	Stereo RGB + PHM	Depth	Depth + PHM	MarLe	NDI
Monocular RGB	—							
Monocular RGB + PHM	0.0840	—						
Stereo RGB	1.0000	0.0840	—					
Stereo RGB + PHM	1.0000	0.0840	1.0000	—				
Depth	<0.0001	0.0077	<0.0001	<0.0001	—			
Depth + PHM	1.0000	0.1911	1.0000	1.0000	<0.0001	—		
MarLe	<0.0001	<0.0001	<0.0001	<0.0001	<0.0001	<0.0001	—	
NDI	0.0023	0.0961	0.0023	0.0023	0.0046	0.0012	<0.0001	—

Table S.6: Post-hoc pairwise comparisons for failure rate ( $p$ -values), corresponding to tracking method ranking in Table 1.